# Performance Evaluation of Hypersonic Turbojet Experimental Aircraft Using Integrated Numerical Simulation with Pre-cooled Turbojet Engine

*Hidemasa Miyamoto and Akiko Matsuo*
*Keio University, Yokohama, Kanagawa, 223-8522 JAPAN, mr061915@hc.cc.keio.ac.jp*
*and*
*Takayuki Kojima and Hideyuki Taguchi*
*Japan Aerospace Exploration Agency, Chofu, Tokyo, 182-8522 JAPAN*

*Keywords: Propulsion, turbojet engine, plug nozzle, linearspike nozzle, aerospike nozzle, CFD*

## Abstract

The effect of Pre-cooled Turbojet Engine installation and nozzle exhaust jet on Hypersonic Turbojet EXperimental aircraft (HYTEX aircraft) were investigated by three-dimensional numerical analyses to obtain aerodynamic characteristics of the aircraft during its in-flight condition.

First, simulations of wind tunnel experiment using small scale model of the aircraft with and without the rectangular duct reproducing engine was performed at M=5.1 condition in order to validate the calculation code. Here, good agreements with experimental data were obtained regarding centerline wall pressures on the aircraft and aerodynamic coefficients of forces and moments acting on the aircraft.

Next, full scale integrated analysis of the aircraft and the engine were conducted for flight Mach numbers of M=5.0, 4.0, 3.5, 3.0, and 2.0.

Increasing the angle of attack $\alpha$ of the aircraft in M=5.0 flight increased the mass flow rate of the air captured at the intake due to pre-compression effect of the nose shockwave, also increasing the thrust obtained at the engine plug nozzle. Sufficient thrust for acceleration were obtained at $\alpha =$ 3 and 5 degrees.

Increase of flight Mach number at $\alpha =$ 0 degrees resulted in decrease of mass flow rate captured at the engine intake, and thus decrease in thrust at the nozzle. The thrust was sufficient for acceleration at M=3.5 and lower cases.

Lift force on the aircraft was increased by the integration of engine on the aircraft for all varying angles of attack or flight Mach numbers. However, the slope of lift increase when increasing flight Mach number showed decrease as flight Mach number reach to M=5.0, due to the separation shockwave at the upper surface of the aircraft.

Pitch moment of the aircraft was not affected by the installation of the engines for all angles of attack at M=5.0 condition. In low Mach number cases at $\alpha =$ 0 degrees, installation of the engines increased the pitch moment compared to no engine configuration.

Installation of the engines increased the frictional drag on the aircraft, and its percentage to the total drag ranged between 30-50% for varying angle of attack in M=5.0 flight.

## I. Introduction

After the retirement of the supersonic aircraft Concorde, engineers around the globe have still been longing for a new passenger aircraft fly back to sky beyond the sound limit. Japanese engineers are no exception, and as a new means of fast, reliable, and environmentally safe transportation, next generation hypersonic aircraft is now being researched and developed. There exist numerous difficulties to overcome to achieve such a goal, and improvement of the propulsive technology is one of the most important issues.

In order to obtain a new suitable engine for successive and efficient flight of hypersonic aircraft, Pre-cooled Turbojet Engine is being developed. Figure 1 shows the structure schematic of its prototype. The engine is an air breathing type in which utilizes liquid hydrogen fuel to be combusted in a 2-stage combustion cycle. The cold fuel is also used as a cooling medium to cool the high temperature compressed air captured from the rectangular intake by flowing through the precooler as indicated in the figure. Since the engine requires a capability to operate from still and subsonic to hypersonic condition in a wide range of flight altitude, a plug nozzle is selected as a nozzle to accelerate the combusted gas in the engine and give thrust to the aircraft.

Currently, the development of the Pre-cooled Turbojet Engine is in a stage of on-ground tests and CFD analyses. The next stage on focus is the in-flight test at hypersonic speed, and the engine is to be installed on the Hypersonic Turbojet EXperimental aircraft (HYTEX aircraft) and tested in the procedure shown in Fig. 2 using a solid rocket booster launch system. For this reason, flight characteristics of the HYTEX aircraft considering engine and its exhaust jet need to be estimated to establish a successful operation control.

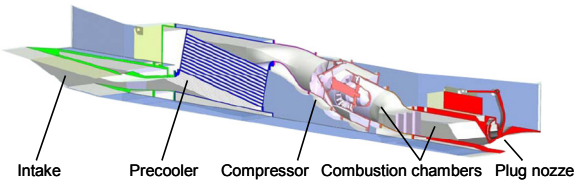


Fig. 1 Structure schematic of the Pre-cooled Turbojet Engine.

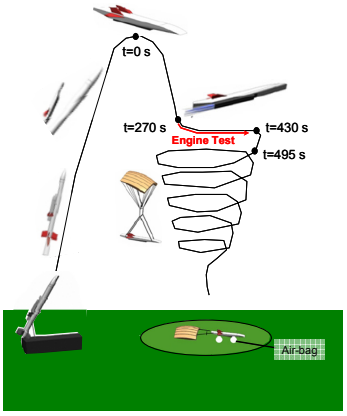


Fig. 2 Procedures for HYTEX engine test.

The objective of this research is to numerically investigate the effects of engine installation and nozzle exhaust jet on the aerodynamic characteristics of the HYTEX aircraft and vice versa. First, simulation of small scale HYTEX wind tunnel experiment is conducted to validate the three-dimensional multi-species code used in the main analyses. Then, full scale analyses were conducted to evaluate the in-flight characteristics of the aircraft along with the performances of engine intake and plug nozzle.

## II. Computational Target

### A. Simulation of Wind Tunnel Experiment

Figure 3 shows the draft diagram of the 1/10 scale wind tunnel model of the HYTEX aircraft. The wind tunnel experiment was performed by Taguchi, *et al*[1-2]. Calculations have been conducted for configurations with and without the rectangular flow-through duct on the lower side of the aircraft to simulate engine. The flow condition is focused on $M_\infty = 5.1$, $P_{0,\infty} = 1.0\,MPa$, and $T_{0,\infty} = 700K$ condition at angle of attack $\alpha$ from -6 to 6 degrees.

In the experiment, pressure is measured at the static holes located on the upper and lower surfaces of the aircraft along the center symmetric line (y=0). Forces in x and z axis direction and moment around y axis acting on the model are also measured in the experiment using the 1/20 scale model, and are evaluated as aerodynamic coefficients by non-dimensionalizing the values as follows.

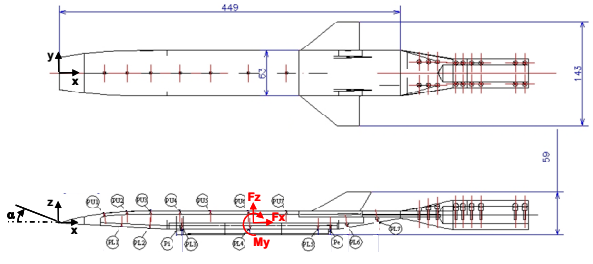


Fig. 3 1/10 Scale HYTEX wind tunnel model.

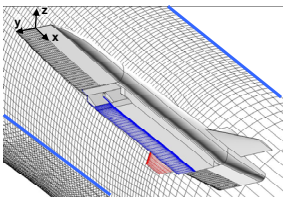

(a) Perspective view

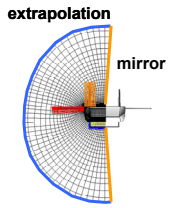


(b) Front view

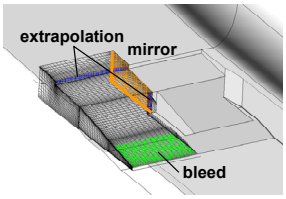


(c) Intake

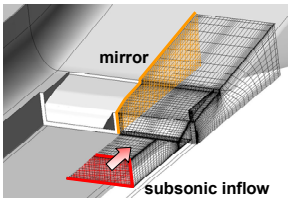


(d) Plug nozzle

Fig. 4 HYTEX aircraft and the computational grids.

$$\begin{cases} C_{F_i} = \dfrac{F_i}{\frac{1}{2}\rho_\infty u_\infty^2 A_{model}} \\ C_{M_i} = \dfrac{M_i}{\frac{1}{2}\rho_\infty u_\infty^2 A_{model} L_{model}} \end{cases} \quad i = x, y, z \qquad (1)$$

Here, $A_{model}$ and $L_{model}$ are the area of the tail base and x direction length of the aircraft model respectively.

### B. Full Scale Analyses of HYTEX aircraft

Figure 4 shows the HYTEX aircraft in which the target of the present analyses is aimed at, along with the computational grid described in the next section. The aircraft has a lifting body configuration and has pairs of horizontal and vertical stabilizers at the tail of the aircraft. Two Pre-cooled Turbojet Engines are installed on the lower side of the aircraft.

The main flight condition that is focused on in this study is of flight Mach number M=5.0 at 24km altitude atmosphere, angle of attack $\alpha$ ranging between -5 to 5 degrees. Analyses for M=2.0, 3.0, 3.5, and 4.0 conditions have also been conducted for 0 degrees angle of attack. Table 1 lists the details of the above conditions.

Figure 5 shows the schematic for explaining the treatment of engine intake and nozzle geometry configuration. In order to obtain enough compressed air at the intake suitable for combustion, intake geometry configuration is varied by adjusting the ramp angle $\theta$ as shown in the figure. Once the mass flow rate $\dot{m}_{air}$ of the captured air is obtained by conducting certain amount of iterations, nozzle throat area is adjusted to satisfy the following quasi one-dimensional isentropic equation for internal flow[3].

$$A^* = \frac{\dot{m}}{p_0}\sqrt{\frac{RT_0}{\gamma\left(\frac{2}{\gamma+1}\right)^{\frac{\gamma+1}{\gamma-1}}}} \qquad (2)$$

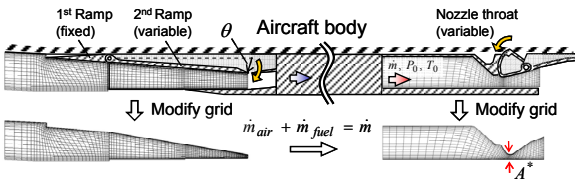


Fig. 5 Treatment for engine geometry configuration.

In the above equation, the total mass flow rate $\dot{m}$ is the sum of $\dot{m}_{air}$ and the mass flow rate of the fuel $\dot{m}_{fuel}$. For each of the flight Mach numbers, total pressure $P_0$ and the total temperature $T_0$ in the combustion chamber are kept constant in the values listed in Table 2. Further details regarding engine conditions are also listed in the table.

Aerodynamic coefficients of forces and moments are also evaluated in these analyses using Eq.(1). Here, the standard area and length used for non-dimensionalization are replaced by $A = 2.804\,m^2$ and $L = 4.5m$.

Table 1 Flight conditions

| Flight Mach | α, deg. | Alt., km | $P_a$, kPa | $T_a$, K | Dynamic pressure, kPa |
|---|---|---|---|---|---|
| 2.0 | 0 | 12.5 | 17.9 | 217 | |
| 3.5 | 0 | 19.7 | 5.9 | 217 | 50 |
| 5.0 | -5 ~ 5 | 24.0 | 2.9 | 221 | |

Table 2 Engine conditions

| Flight Mach | Intake ramp angle θ, deg. | Fuel mass flow rate, kg/s | $P_0$, kPa | $T_0$, K | Mol. Fraction ($N_2$, $H_2$, $H_2O$) |
|---|---|---|---|---|---|
| 2.0 | 6.5 | 0.066 | 345 | 2,037 | 0.512, 0.221, 0.267 |
| 3.5 | 11.0 | 0.057 | 317 | 2,083 | 0.479, 0.271, 0.250 |
| 5.0 | 12.2 | 0.061 | 283 | 2,078 | 0.416, 0.367, 0.217 |

## III. Computational Setup

The governing equations solved in the present study are three-dimensional Navier-Stokes equations and equations for species mass conservation of $N_2$, $H_2$, $O_2$, and $H_2O$. Since the aircraft geometry configuration is complicated, the present analyses utilize an overset grid method. For this reason, the governing equations contain fortifying solution terms based on Fortifying Solution Algorithm[4] (FSA). The numerical scheme used is 3rd order Simple High-Resolution Upwind Scheme[5] and 2nd order central difference method for convective and viscous terms respectively. For time integration, Lower-Upper Alternating Direction Implicit Scheme[6-7] is adopted. To appropriately estimate the flowfield of turbulent boundary layers, Baldwin-Lomax turbulence model[8] is also adopted.

Figure 4 shows the set of computational grids used in the analyses along with the boundary conditions. Total number of nodes sum up to 6 million, and the grid spacing near the wall is dense for conducting viscous calculation. Symmetric boundary

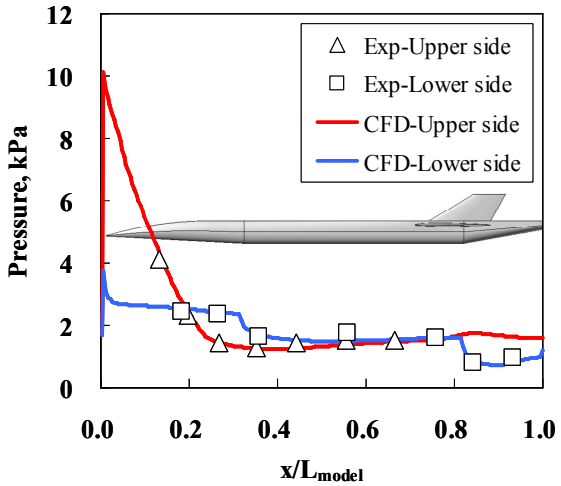


Fig. 6 Surface pressure distributions along the symmetric plane (W/O engine duct).

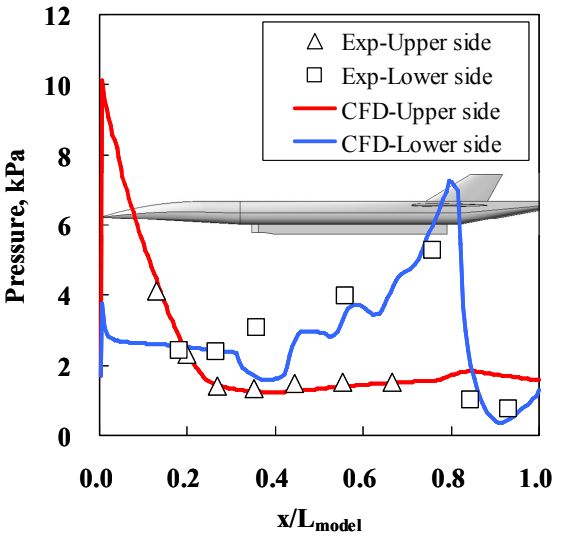


Fig. 7 Surface pressure distributions along the symmetric plane (W/ engine duct).

condition is applied on the boundaries at y=0 plane so that the size of the computational domain is reduced to half of the actual size. To avoid the intake unstart phenomenon due to separation of boundary layer at intake, bleed condition is applied at the indicated ramp surface by explicitly specifying the velocity normal to the surface. The specified velocities are 30 m/s for M=2.0, 90 m/s for M=3.0-4.0, and 150 m/s for M=5.0 conditions.

## IV. Results and Discussion

### A. Simulation of Wind Tunnel Experiment

Figure 6 shows the pressure distribution along the upper and lower surface of the aircraft at the symmetric plane y=0, for the no engine configuration at an angle of attack $\alpha = 0$ degrees. The values are compared with the experimental data and are in good agreement with each other. It can also be observed that the expansion on the lower downstream surface between $x/L_{model}$=0.8 to 1.0 was reproduced well using the turbulence model currently applied, which was not reproduced in the laminar calculation. The results for $\alpha$ = -5, -3, 3, and 5 degrees are not printed

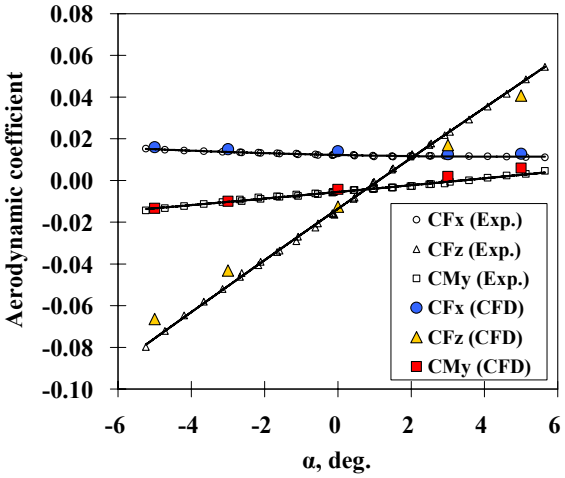


Fig. 8 Aerodynamic coefficients for the simulation of wind tunnel experiment (W/O engine duct).

on this p aper but were also done, and they all showed good agreement with the experimental data similarly.

Figure 7 shows the pressure distribution similarly as in Fig. 6 for the configuration with the rectangular flow-through duct simulating engine, at $\alpha = 0$ degrees. Here, the pressure distribution along the lower surface includes the pressures measured inside the duct. The pressure distribution on the upper surface agree well with the experimental data, however a clear difference on the lower surface can be observed inside the engine duct. The behaviors of pressure change in the present analysis and experiment show opposite tendency at the duct inlet near $x/L_{model}$=0.35. A possibility may be considered that in the experiment, the boundary layer inside the duct was disturbed and thickened by the shockwave formed around the pitot tube located at the duct inlet. This may have led the high pressure in the downstream region to propagate upstream, giving the experimental result as plotted in the figure. On the other hand, since the pitot tube does not exist in the numerical analysis, the flow simply expanded along the body inflection point at $x/L_{model}$=0.32 and then was compressed by the oblique shockwaves formed around the rims of the duct inlet. The pressure intermittently continued to rise due to the reflections of these shockwaves, and then furthermore increased since the growing boundary layers decreased the effective cross sectional area of the duct, turning the duct into a supersonic diffuser to compress the flow captured from the inlet.

Figure 8 shows the comparison of the aerodynamic coefficients for configuration without the engine duct, varying the angle of attack $\alpha$. Here $C_{Fx}$, $C_{Fz}$, and $C_{My}$ indicate drag, lift, and pitch moment respectively. It can be seen that the computational results match well with the experimental data. From the above results regarding the analyses simulating the HYTEX wind tunnel experiment, it can be concluded that the present three-dimensional multi-species code is validated for use in the main analyses in the next section.

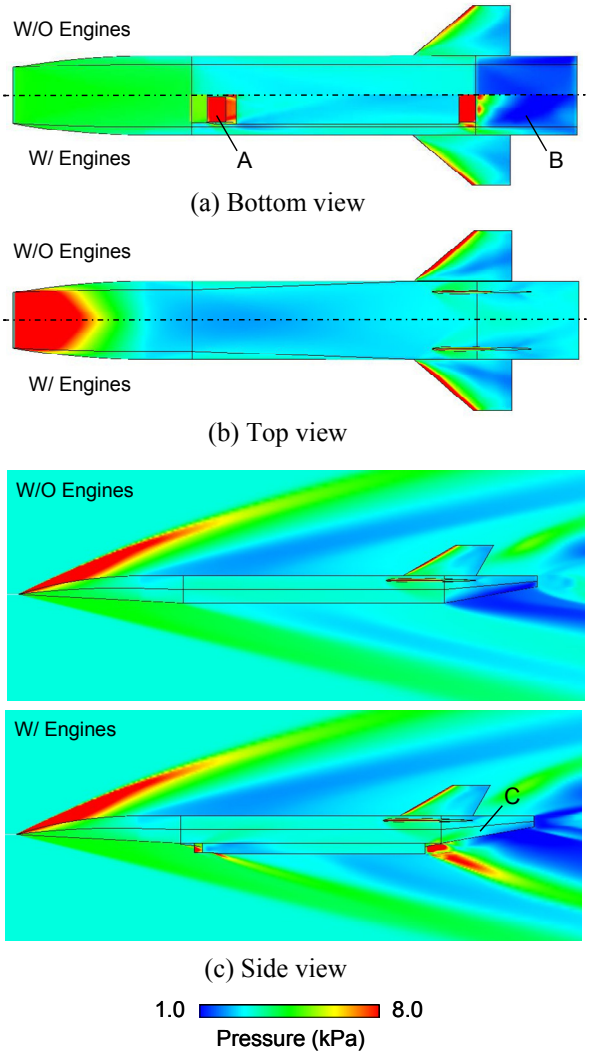


Fig. 9 Effect of engine installation on the flowfield ; Pressure distributions on aircraft surface and y=0 plane for M=5.0 at α=0 degrees.

## B. Full Scale Analyses of HYTEX aircraft

### Flowfield

Figure 9 (a)-(c) show the comparison of pressure distributions on aircraft surface for configurations with and without engines at M=5.0 and $\alpha = 0$deg. The side view images also include the pressure distributions of symmetric plane y=0. For the configuration with the engines installed, it can be observed that the high pressure is acting on the intake ramp surfaces due to compression, indicated by the letter 'A' in the bottom view image. At the nozzle ramp surface also exists high pressure region due to the exhaust jet flowing along it. However the exhaust jet keeps expanding along the bottom tail surface to pressure lower than the ambient value creating drag. (Indicated by the letter 'B' in the image)

As indicated by the letter 'C' in Fig. 9, the expansion at the downstream sidebody is suppressed in the case with the engines. This is because the flow from the side of the body cannot flow into the bottom tail region since the exhaust jet blocks its way.

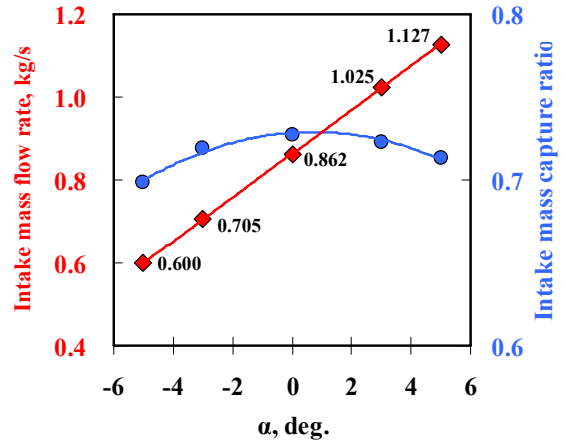


(a) For M=5.0 with varying angle of attack

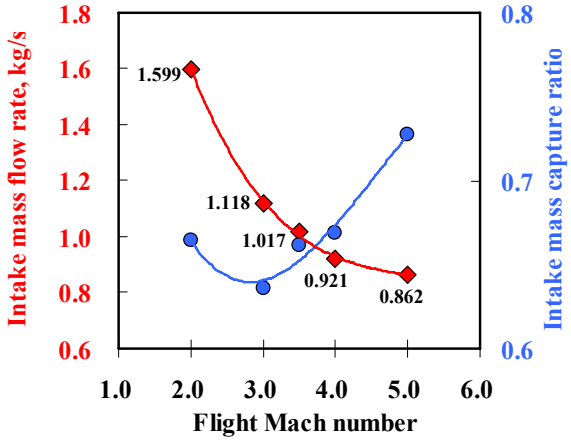


(b) For α=0 degrees with varying flight Mach

Fig. 10 Intake mass flow rate and mass capture ratio.

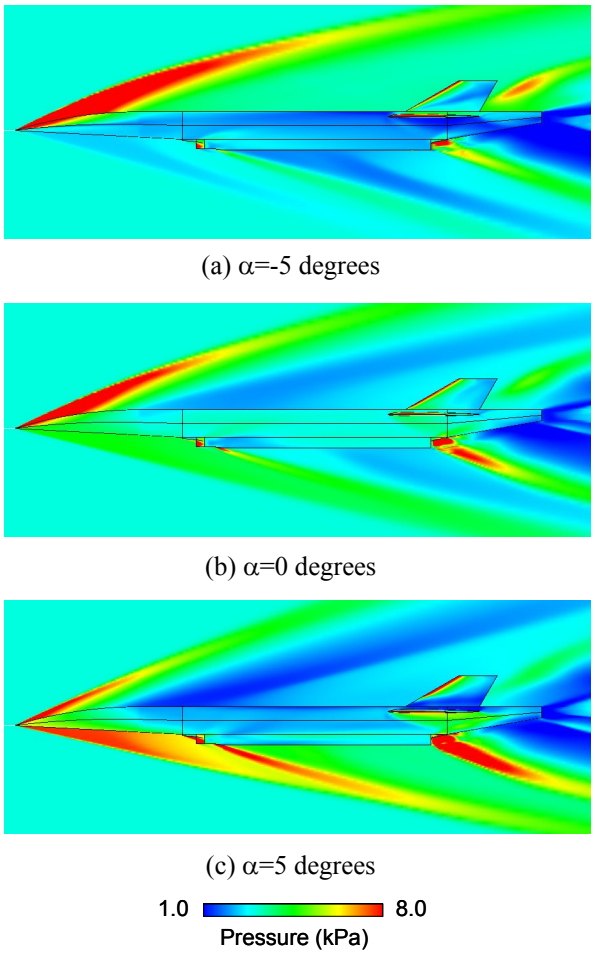


Fig. 11 Effect of engine installation on the flowfield ; Pressure distributions on aircraft surface and y=0 plane for M=5.0 with varying angle of attack.

Comparing the overall pressure distributions on the upper surfaces, there was no remarkable effect of engine installation on the upper side of the aircraft.

**Intake Performance**

It is important that the intake capture sufficient amount of air for successive combustion so that the engine produces enough thrust for aircraft acceleration. Figure 10 (a) shows the mass flow rate of air captured at the inlet of the engine, plotted against the angle of attack for M=5.0 condition. Mass capture ratio (MCR, the relative ratio of mass flow rate compared to the value at the most upstream section of the intake ramp) is also plotted on the figure using the second vertical axis. From the figure, it can be observed that the mass flow rate increases linearly with the increasing angle of attack, and it is to note that the value almost doubles in the $\alpha =$ 5 degrees case compared to the $\alpha =$ -5 degrees case. A relative maximum exists for MCR at $\alpha = 0$ degrees, however the overall range of change is small and the MCR may be considered almost constant for varying angle of attack. Therefore, the reason for the above increase in the mass flow rate is the pre-compression of the air by the oblique shockwave at the nose of the aircraft body. Figure 11 (a)-(c) show the pressure distribution of the symmetric plane y=0 for $\alpha =$ -5, 0, and 5 degrees in M=5.0 condition. Here it can be observed that the state of the air just in front of the intake varies very much for different angles of attack due to the compression by the oblique shockwave.

Figure 10 (b) shows the mass capture ratio and the MCR of the intake plotted against the flight Mach number, in which all cases are of $\alpha = 0$ degrees. The mass flow rate captured decreases with increasing flight Mach number since the air density decreases with the increasing altitude. On the other hand, MCR has a relative minimum at M=3.0 and then increases as the flight Mach number increases. This is because for M=2.0 case, the 1st ramp and the 2nd ramp are aligned in a straight line and only a single oblique shockwave is formed at the tip of the 1st ramp. For cases of M=3.0 and higher, a second shockwave is formed at the 2nd ramp in which its angle is varied, resulting in further spillage. Figure 12 shows the MCR values at intake cross sections for each flight Mach numbers at $\alpha = 0$ degrees, graphed against the x direction distance. For all three cases, the MCR continues to decrease almost at the same rate up to x/L=0.335, where spillage can be seen for the M=2.0 case due to oblique shockwave formed at the tip of the 1st ramp. For higher Mach numbers, the starting

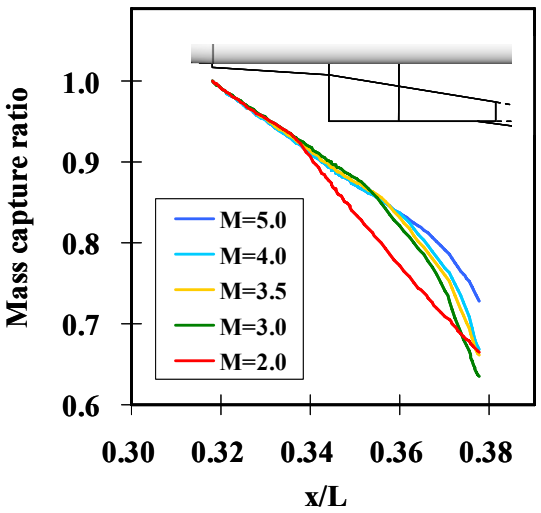


Fig. 12 Change of intake mass capture ratio in streamwise direction (α=0 degrees).

point of this spillage is shifted towards downstream since the angle of this shockwave becomes more acute with the increasing flight Mach number.

**Nozzle Performance**

Figure 13 (a) shows the nozzle thrust values in M=5.0 condition plotted against the varying angle of attack. Here the gross thrust values indicate the thrust of the nozzle itself. The net thrust values are the total thrust of the engine in which the forces acting on the intake is subtracted from the gross thrust values. Due to the increasing captured mass flow at the intake, the gross and net thrust increases with the increasing angle of attack as well. However, the slope for the change of net thrust is much gentle compared to that of gross thrust. This indicates that the ratio of drag force acting on the intake to the total thrust is increasing with the increase of angle of attack.

Figure 13 (b) shows the nozzle thrust values plotted against the flight Mach number for $\alpha = 0$ degrees. The broken lines in the figure indicate the thrust values obtained from the independent analyses of the engine. From this figure, it can be observed that when the flight Mach number becomes low, the thrust values in the present integrated analyses part from the values from the independent analyses of engine. This is because in lower Mach numbers, the shockwave standing at the nose of the aircraft becomes much closer to normal shockwave. This results in a remarkable pre-compression effect of the air flowing to the intake, and thus the total mass flow rate and the thrust of the engine is increased.

**Aerodynamic Performance of the Aircraft**

Figure 14 (a)-(c) show the aerodynamic coefficients for the entire aircraft system of HYTEX at M=5.0 condition, plotted against the angle of attack. The values on these figures are compared with the values of the no engine configuration. Regarding the drag coefficient $C_{Fx}$, the positive values indicate insufficient thrust to the aircraft. It can be seen that for the present configuration, the aircraft must take an angle of attack greater than 3 degrees in order to

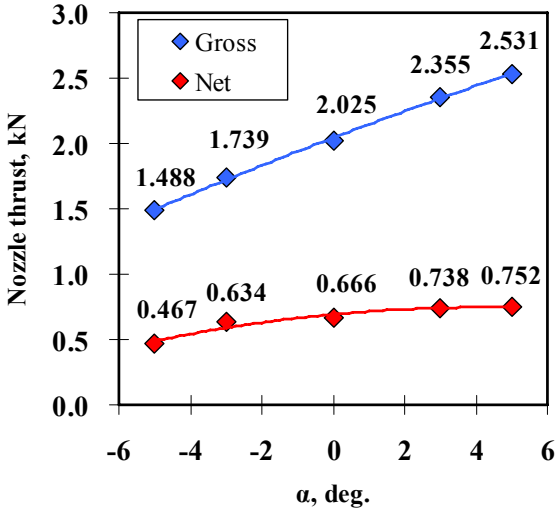


(a) For M=5.0 with varying angle of attack

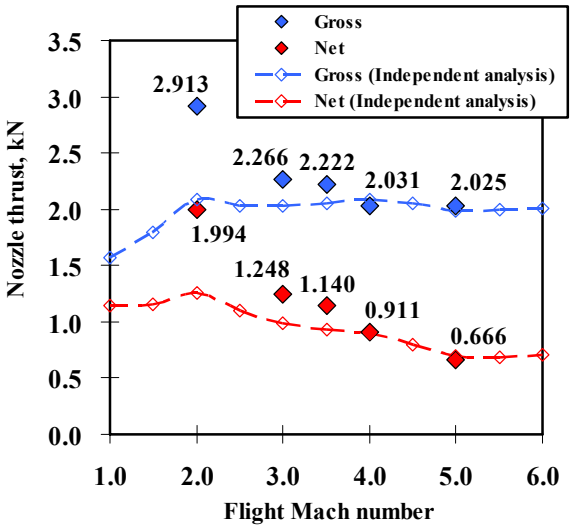


(b) For α=0 degrees with varying flight Mach

Fig. 13 Nozzle thrust.

gain acceleration.

For the lift coefficient $C_{Fz}$ in Fig. 14 (b), installation of engine shifts the overall plot to the positive direction. This is mainly due to the z direction force obtained from the high pressures at intake and plug nozzle ramp.

Observing the pitch moment coefficient $C_{My}$ in Fig. 14 (c), it can be seen that the installation of engine does not affect the pitch balance behavior. However the pitch increases with the increasing angle of attack, and this indicates that the lift force acting on the body upstream of the aerodynamic center is becoming larger than that of the downstream. Furthermore, the zero-pitch position in which the aircraft is stable is at around 2 degrees for the current configuration, and this indicates the need that the aerodynamic center be shifted forward by applying such improvement as modifying the geometry of horizontal stabilizer so that more lift force could be obtained at the downstream half of the aircraft.

Figure 15 (a)-(c) similarly show the aerodynamic coefficients of the aircraft for varying flight Mach numbers at $\alpha = 0$ degrees. Observing the drag

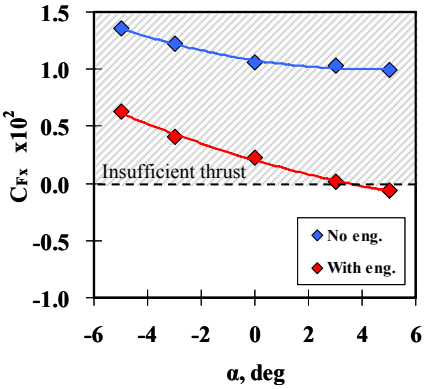


(a) Drag $C_{Fx}$

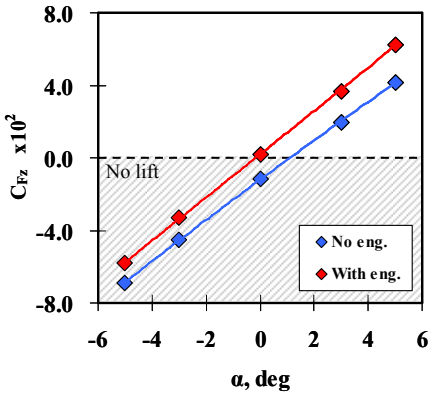


(b) Lift $C_{Fz}$

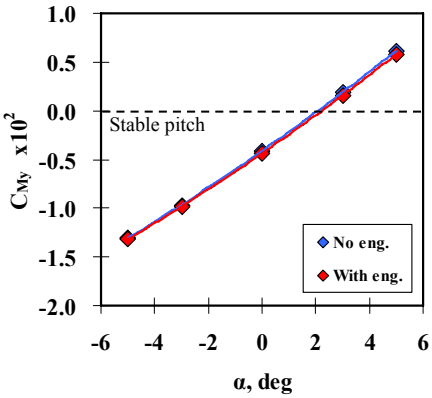


(c) Pitch moment $C_{My}$

Fig. 14 Aerodynamic coefficients for M=5.0 with varying angle of attack.

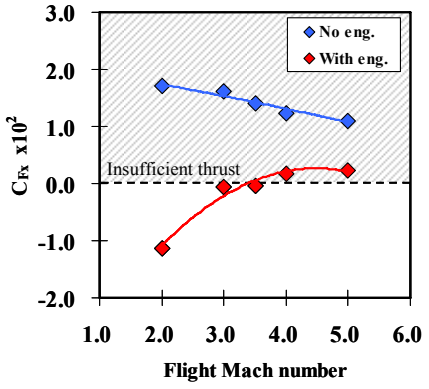


(a) Drag $C_{Fx}$

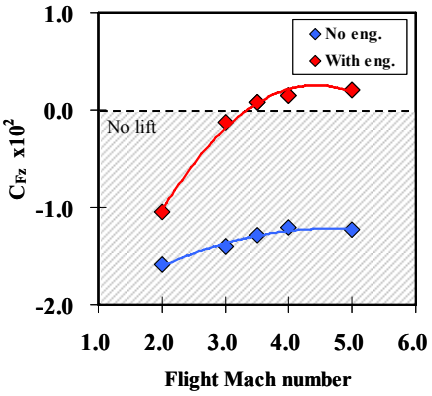


(b) Lift $C_{Fz}$

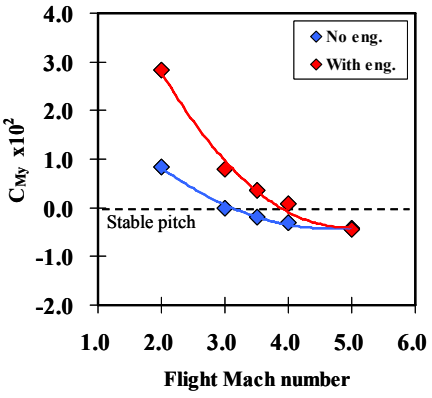


(c) Pitch moment $C_{My}$

Fig. 15 Aerodynamic coefficients for α=0 degrees with varying flight Mach number.

coefficient $C_{Fx}$ in Fig. 15 (a), while acceleration was not obtained for the cruising M=5.0 case, in cases of M=3.5 and below the aircraft was able to obtain sufficient thrust for acceleration when the engines were installed.

Regarding the lift coefficient $C_{Fz}$ in Fig. 15 (b), negative estimates were obtained for all cases of no engine configuration. The lift values were increased by installation of the engines and positive lift forces were achieved for M=3.5-5.0 cases. Another element to be noted is that the rates of change of lift coefficients against increasing flight Mach numbers are decreasing as the Mach number get close to M=5.0. Since this tendency applies for both configurations with and without the engines, its cause must be in the flowfield of the upper side of the aircraft. Figure 16 (a) and (b) respectively show the Mach number and pressure distributions on the y=0 plane for no engine configuration at M=5.0 and $\alpha = 0$ degrees. Here, a largely grown boundary layer can be seen on the upper side of the aircraft. The boundary layer is not quite separated yet, however a separation shockwave stands over it to increase the pressure of the upper downstream surface of the aircraft. This results in a downward force to act on the body and this is the reason for the above tendency of lift decrease. This large scale boundary layer is only seen in the M=3.0 and higher conditions, and its cause is possibly the interaction of the shockwaves from the two vertical stabilizers formed above the upper downstream surface of the aircraft. Since high pressure region is formed by the interaction, the boundary layer is thickened due to the adverse pressure gradient. From the above discussion,

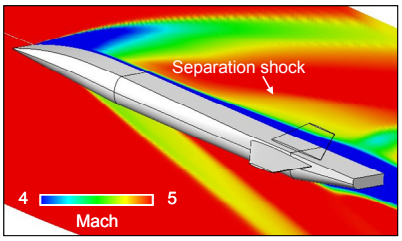


(a) Mach number distribution

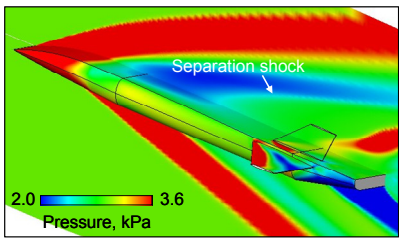


(b) Pressure distribution

Fig. 16 Grown boundary layer on the upper surface of the aircraft at M=5.0, α=0 degrees.

countermeasures such as varying the stabilizer angles or parting the two stabilizers must be taken so that the boundary layer separation is suppressed in hypersonic flight Mach numbers.

From the coefficient of pitch moment $C_{My}$ in Fig. 15 (c), it can be noted that the values of configurations with and without the engines become close to each other with the increase of flight Mach number. The flight Mach number in which stable pitch ($C_{My}$=0) is obtained at $\alpha = 0$ degrees may be estimated to be around M=4.0.

Figure 17 (a) shows the frictional drag of the aircraft plotted against the angle of attack at M=5.0. The values in the parenthesis indicate the percentage of frictional drag compared to the overall drag on the aircraft (excludes the forces on engine inlet and outlet). By installing the engines onto the aircraft, the overall frictional drag increases due to the increase in the exposed surface area. For the no engine configuration, a clear minimum value can be observed at $\alpha = 0$ degrees. It can also be noted that the percentage of frictional drag ranges between 30-50% for the configuration with the engines, and 20-40% for the configuration without the engines.

Figure 17 (b) similarly shows the frictional drag plotted against the flight Mach numbers at $\alpha = 0$ degrees. Relative maximums at M=3.0 and tendencies of decrease at higher Mach numbers were observed for both configurations with and without the engines. The cause for such decrease is the largely grown boundary layer on the upper surface of the aircraft mentioned above and shown in Fig. 16 at M=3.0 and higher cases. Since the velocity gradient normal to the wall surface is decreased by the formation of large boundary layer, the friction decreased in large part of the upper body surface.

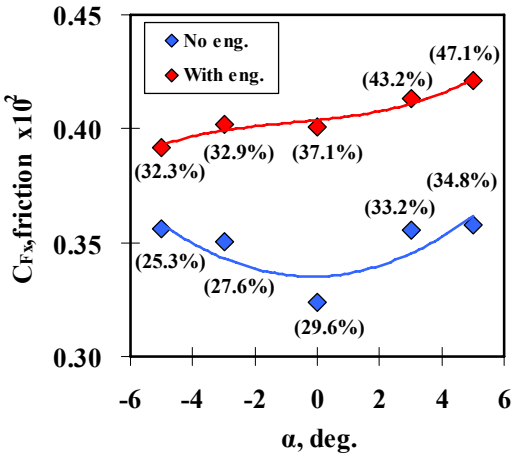


(a) For M=5.0 with varying angle of attack

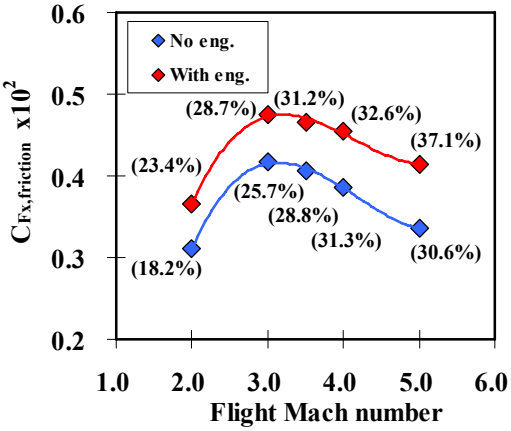


(b) For α=0 degrees with varying flight Mach number

Fig. 17 Frictional drag coefficient on the aircraft. (The values in parenthesis indicate the percentage of frictional drag compared to the total drag force on the aircraft.)

## V. Conclusion

Integrated numerical analyses of HYTEX aircraft and Pre-cooled Turbojet Engine were performed using three-dimensional multi-species code.

First, validation of the calculation code was conducted by simulating the wind tunnel experiment of small scale HYTEX model. The pressure distributions along the centerline wall surface and the aerodynamic coefficients of lift, drag, and pitch moment agreed well with the experimental data.

Next, full scale simulations were conducted and following evaluations were made regarding the in-flight performances of the aircraft.

- Increasing the angle of attack in M=5.0 flight increased the mass flow rate of the air captured at the intake due to pre-compression by the nose shockwave, increasing the thrust obtained at the engine plug nozzle. Sufficient thrust for acceleration at M=5.0 were obtained at $\alpha = 3$ and 5 degrees.

- Increase of flight Mach number at $\alpha = 0$ degrees resulted in decrease of mass flow rate captured at the engine intake, and thus decrease in thrust at the nozzle. The thrust was sufficient for acceleration at M=3.5 and lower cases.
- Lift force on the aircraft was increased by the integration of engine on the aircraft for all varying angles of attack or flight Mach numbers. However, the slope of lift increase when increasing flight Mach number showed decrease as flight Mach number reach to M=5.0, due to the separation shockwave at the upper surface of the aircraft.
- Pitch moment of the aircraft was not affected by the installation of the engines for all angles of attack at M=5.0 condition. In low Mach number cases at $\alpha = 0$ degrees, installation of engines increased the pitch moment compared to no engine configuration.
- Installation of the engines increased the frictional drag on the aircraft, and its percentage to the total drag ranged between 30-50% for varying angle of attack in M=5.0 flight.

## Ackknowledgment

Special acknowledgement is given to the Institute of Space and Astronautical Science of Japan Aerospace Exploration Agency as the calculations in this study were performed using NEC SX-6 high performance computer (Space Science Simulator, SSS) in the facility.

## References

1) Taguchi, H., *et al*, "Wind Tunnel Experiment of Hypersonic Aircraft", Proceedings of the 38th Conference of Fluid Dynamics, Japan, 2006 [In Japanese]
2) Nakatani, H., "Effect of Flow around Engines on Aerodynamic Performance of a Mach 5-Class Hypersonic Airplane", Tokyo University of Science Graduation Thesis (Faculty of Technology, Department of Mechanical Engineering), 2007 [In Japanese]
3) Matsuo, K., "Compressible Fluid Dynamics", Rikogakusha, 1994 [In Japanese]
4) Fujii, K., "Unified Zonal Method Based on the Fortified Solution Algorithm", *Journal of Computational Physics*, 118, 1995, pp.92-108
5) Shima, E. and Jounouchi, T., "Role of Computational Fluid Dynamics in Aeronautical Engineering (No. 12), Formulation and Verification of Uni-Particle Upwind Schemes fort the Euler Equations", Proceedings of the 12th NAL Symposium on Aircraft Computational Aerodynamics, Japan, 1995, pp.255-260 [In Japanese]
6) Obayashi, S. and Kuwahara, K., "An Approximate LU Factorization Method for the Compressive Navier-Stokes Equations", *Journal of Computational Physics*, 63, 1986, pp.157-167
7) Obayashi, S., Matsushima, K., Fujii, K., and Kuwahara, K., "Improvements in Efficiency and Reliability for Navier-Stokes Computations using the LU-ADI Factorization Algorithm", AIAA Paper, 86-338
8) Wilcox, D.C., "Turbulence Modeling for CFD", DCW Industries, 1998, pp1-185